Influence of Unidirectional Power Flow and Restoring Force Absence on Wavepiston Performance

Eugenio M. Gelos, Pedro O. Fornaro, Colm J. Fitzgerald, and John V. Ringwood

Abstract—**Wavepiston is a novel wave energy converter (WEC) comprising multiple energy collectors coupled on a string, each equipped with a sail designed to harness surge excitation from incoming waves. The current configuration features two distinctive design characteristics that significantly influence its hydrodynamic behavior and control: (i) a passive Power Take-Off (PTO) enabling only unidirectional power flow, and (ii) the absence of hydrodynamic restoring capabilities. Despite recent technological progress and a high technology readiness level, limited attention has been given to implementing state-of-the-art control strategies for this device, particularly evaluating how its unique design features influence overall performance. Therefore, this preliminary study aims to evaluate how unidirectional power flow imposed by the passive PTO and the absence of restoring capabilities influence the following performance metrics: (i) power capture across various sea states, (ii) operational spaces of sail stroke and (iii) PTO control force, along with (iv) energy production in a specific wave climate. The results provide a basis for identifying performance trade-offs and support the evaluation of potential design pathways accounting for both device dynamics and wave climate characteristics.**

Index Terms—**Wavepiston, Performance Assessment, Optimal Control, Power Constraints, Wave Energy**

I. Introduction

WAVEPISTON is a novel wave energy converter (WEC) that consists of multiple energy collectors coupled together on a string [1], as depicted in Figure 1a-1b. Each collector includes a sail, designed to harness the surge excitation from incoming waves and a hydraulic power take-off (PTO). To date, Wavepiston has achieved significant technological milestones, including the recent installation of 3rd generation device at the PLOCAN offshore facilities in Gran Canaria [2], where testing is being conducted to evaluate the overall performance of the device. Insights gained from this experimental testing will inform future design refinements for an upgraded full-scale device intended for potential deployment on the northern side of Gran Canaria.

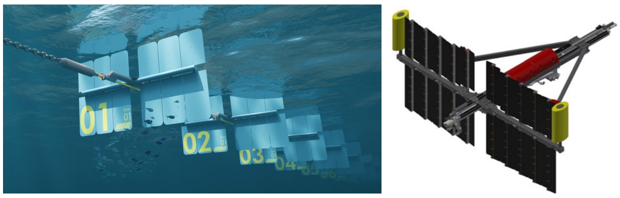

(a) (b)

Fig. 1: (a) Schematic illustration of the Wavepiston device, comprising multiple energy collectors coupled along a string. (b) Detail of a single energy collector, equipped with a sail and a hydraulic PTO designed to harness surge excitation from incoming waves.

Interestingly, the baseline configuration of the Wavepiston device features two distinctive design characteristics that have significant implications for both its hydrodynamic behavior and control. First, in its current baseline configuration, the PTO is passive, meaning it allows only unidirectional power flow, preventing power transmission from the PTO to the energy collector. Second, since the sails are constrained to move horizontally and are assumed rigid, no hydrodynamic restoring force acts on the WEC. The lack of restoring force distinguishes Wavepiston from most established WEC concepts that operate as resonant systems with inherent self-centering capabilities, such as point absorbers and oscillating wave surge converters.

Wavepiston efforts have primarily focused on technological development, achieving significant advancement on its technology readiness level (TRL) index [1]. In the light of this, several studies have leveraged its high TRL, using the Wavepiston device as a case study, to develop and implement WEC-to-site pairing techniques, and to conduct analyses for specific applications, such as desalination plants, with a strong emphasis on evaluating various economic factors [3]–[12]. Moreover, some performance assessments of Wavepiston device have been conducted, mainly through experimental testing on offshore platforms [2], or in wave tanks [13], [14]. Additionally, [15] presents a preliminary performance assessment, based on simulation of the Wavepiston device using simple modelling techniques and monochromatic wave scenarios.

Therefore, to the best of the authors' knowledge, limited attention has been given to the application of state-of-the-art control strategies to the Wavepiston device, particularly regarding how its unique design

Part of a special issue for EWTEC 2025. Original version published in EWTEC 2025 proceedings at doi.org/10.36688/ewtec-2025-964.

This work was supported by the European Union under Horizon funding (Grant Agreement No. 101147456 – SHY), and by Taighde Eireann - Research Ireland under Grant number 21/US/3776.
Eugenio M. Gelos, Pedro O. Fornaro, and Colm J. Fitzgerald are postdoctoral researchers at the Centre for Ocean Energy Research (COER), National University of Ireland, Maynooth (e-mails: eugenio.gelos@mu.ie, pedro.fornaro@mu.ie, and colm.fitzgerald@mu.ie)
John V. Ringwood is the Director of the Centre for Ocean Energy Research (COER), National University of Ireland, Maynooth (e-mail: john.ringwood@mu.ie)
Digital Object Identifier: https://doi.org/10.36688/imej.9.19-28

characteristics affect overall performance. Addressing this gap can provide insight to inform future iterations of the Wavepiston design and improve the development of effective control strategies for this device.

Acknowledging the existing gap in the literature, the main objective of this preliminary study is to evaluate how (a) the passive PTO enforcing unidirectional power flow, and (b) the absence of restoring capabilities in the baseline Wavepiston configuration affect the following performance metrics of the WEC: (i) power capture across various sea states, operational spaces of (ii) the sail stroke and (iii) PTO control force, as well as (iv) energy production in a representative wave climate corresponding to a potential deployment site in northern Gran Canaria. The performance metrics obtained from this analysis are presented in two complementary forms: detailed distributions across sea states and a condensed representation that summarizes the performance of each configuration across the evaluated metrics. This combined presentation enables both a detailed analysis at the sea-state level and a concise comparison of performance trends across configurations. Additionally, the implications of the results for potential design refinement pathways of the Wavepiston device are discussed.

The remainder of the article is organized as follows. Section II outlines the methodology and key considerations for evaluating the performance metrics of the Wavepiston device. Section III presents the Wavepiston modelling approach and the formulation of the optimal control problem (OCP). Section IV introduces the numerical case study based on the wave climate of the selected deployment site in northern Gran Canaria, while Section V presents the corresponding performance analysis.

II. Methodology

To evaluate the influence of (a) the passive PTO enforcing unidirectional power flow and (b) the absence of restoring capabilities on the performance of the baseline Wavepiston configuration, four different WEC configurations, listed in Table I, are considered. Configuration C1 corresponds to the baseline Wavepiston case, which features a passive PTO and no restoring capabilities. The remaining configurations incorporate either a reactive PTO, capable of transmitting power to the energy collectors and enabling bidirectional power flow, or an external spring mechanism that provides restoring force and self-centering capabilities.

The four configurations in Table I are evaluated under the wave climate of northern Gran Canaria, represented by a set of discrete sea states, with the optimal controller computed for each case. Within this framework, the performance of configurations C2, C3, and C4 is systematically assessed relative to the baseline configuration C1. To ensure a representative performance assessment, the key physical constraints of the Wavepiston device are incorporated into the OCP, including limits on the allowable sail stroke and the maximum PTO control force, as well as the unidirectional power flow constraint imposed by the passive PTO in configurations C1 and C2. Importantly,

TABLE I: Evaluated Wavepiston configurations.

	RESTORING CAPABILITIES	
PTO TYPE	No Added Spring	External Spring
Passive	C1	C2
Reactive	C3	C4

the unidirectional power flow constraint is nonlinear, leading to generally nonconvex OCPs whose numerical solution poses significant challenges for the design of computationally efficient control schemes. Notably, the available literature addressing power constraints is more limited than for cases involving linear constraints, such as position and PTO force limits [16].

Although a range of WEC control strategies has been proposed in the literature [17]–[19], not all can accommodate position and control force constraints. Moreover, many approaches rely on reactive power injection from the PTO to the energy collector [20], [21], which is not feasible for the Wavepiston configurations C1 and C2 due to the passive PTO. Consequently, the set of applicable control strategies capable of handling position, force, and power flow constraints is significantly reduced.

In this context, model predictive control (MPC) and MPC-like approaches are well suited for systematic constraint handling in the Wavepiston device [16]. Among these, a spectral formulation [22] is adopted in this study, as it accommodates all relevant constraints while maintaining computational efficiency in solving the associated OCP. Computational efficiency is particularly important in this study, given the large number of simulation runs required across the four configurations and different sea states, as detailed in Section IV.

Finally, although the Wavepiston baseline configuration consists of multiple energy collectors arranged along a string, each equipped with a sail and PTO (see Fig. 1a), the present analysis is restricted to a single energy collector to simplify the problem and enable a clear interpretation of the results. The modelling approach and the formulation of the associated OCP are presented next.

III. Wavepiston Modelling and Optimal Control Problem Formulation

The hydrodynamics of the Wavepiston device, considering a single energy collector with one degree of freedom in surge, can be described by the equation

$$M\ddot{x}(t) + \int_{-\infty}^{t} K(t-\tau)v(\tau)d\tau + S_h x(t) = F_{ex}(t) - F_u(t), \tag{1}$$

where $x(t)$ and $v(t) = \dot{x}(t)$ denote the position and velocity of the sail, respectively, and $M = m_w + m_\infty$ is the total mass, comprising the WEC mass m_w and the infinite-frequency added mass m_∞ due to radiation effects. The term S_h is the hydrostatic restoring coefficient, $K(t)$ is the radiation impulse response function, $F_{ex}(t)$ is the wave excitation force, and $F_u(t)$ is the control force applied by the PTO. Although configurations C1 and C3 have no restoring capability, the term $S_h\, x(t)$ is retained in (1) for consistency, as configurations Ⓒ2 and Ⓒ4 include an external spring, leading to $S_h \neq 0$.

The OCP associated with maximizing energy absorption over a finite time horizon T_0, subject to the WEC physical constraints, can be defined as

$$\max.: \quad \mathcal{J} = \int_0^{T_0} F_u(t)v(t)dt, \tag{2}$$

$$s.t.: \quad |x(t)| \leq x_{max}, \tag{3}$$

$$|F_u(t)| \leq F_{u,max}, \tag{4}$$

$$p_u(t) = F_u(t)v(t) \geq 0, \tag{5}$$

$$\forall t \in [0, T_0].$$

Here, $p_u(t){=}F_u(t)v(t)$ is the instantaneous PTO power, and $\mathcal{J}$ denotes the absorbed energy over the time horizon T_0. The quantities x_{max} and $F_{u,max}$ define the position and control force limits, respectively. The constraint (5) enforces unidirectional power flow, consistent with the passive PTO in configurations Ⓒ1 and Ⓒ2. In configurations Ⓒ3 and Ⓒ4, which employ a reactive PTO, constraint (5) is removed, and the OCP reduces to (2)–(4).

A. Spectral Transcription of the Optimal Control Problem

The infinite-dimensional continuous-time OCP (2)–(5) is transcribed into a finite-dimensional optimization problem using the spectral approach described in [22]. In this formulation, the velocity, excitation force, and control force are approximated using a truncated zero-mean Fourier series:

$$v(t) \approx \quad \tilde{v}(t) = \mathbf{\Phi}(t)\,\boldsymbol{\mathcal{V}}\,, \tag{6}$$

$$F_{ex}(t) \approx \widetilde{F}_{ex}(t) = \mathbf{\Phi}(t)\,\boldsymbol{\mathcal{E}}\,, \tag{7}$$

$$F_u(t) \approx \ \widetilde{F}_u(t) = \mathbf{\Phi}(t)\boldsymbol{\mathcal{U}}\,, \tag{8}$$

where the notation $\widetilde{\square}$ denotes the Fourier approximation of the corresponding continuous-time signal, and $\mathbf{\Phi}(t) \in \mathbb{R}^{1\times N}$ is the vector of basis functions defined as

$$\mathbf{\Phi}(t) = [\boldsymbol{\phi_1}(t), \boldsymbol{\phi_2}(t), ..., \boldsymbol{\phi_{N/2}}(t)]\,. \tag{9}$$

Here, the *n-th* component is represented as the following two-dimensional vector-valued function:

$$\boldsymbol{\phi_n}(t) = [\cos(n\omega_0 t), \sin(n\omega_0 t)]\,, \tag{10}$$

with ω_0 denoting the fundamental frequency of the Fourier series and $n \in \mathbb{N}$ the harmonic number. Additionally, the vectors $\boldsymbol{\mathcal{V}}$, $\boldsymbol{\mathcal{E}}$, and $\boldsymbol{\mathcal{U}}$ contain the corresponding Fourier coefficients for the velocity, excitation force, and control force, respectively, defined as:

$$\boldsymbol{\mathcal{V}} = [\boldsymbol{v_1}, \boldsymbol{v_2}, ..., \boldsymbol{v_{N/2}}]^\top, \quad \text{with} \quad \boldsymbol{v_n} = [v_{n1}, v_{n2}]^\top, \tag{11}$$

$$\boldsymbol{\mathcal{E}} = [\boldsymbol{e_1}, \boldsymbol{e_2}, ..., \boldsymbol{e_{N/2}}]^\top, \quad \text{with} \quad \boldsymbol{e_n} = [e_{n1}, e_{n2}]^\top, \tag{12}$$

$$\boldsymbol{\mathcal{U}} = [\boldsymbol{u_1}, \boldsymbol{u_2}, ..., \boldsymbol{u_{N/2}}]^\top, \quad \text{with} \quad \boldsymbol{u_n} = [u_{n1}, u_{n2}]^\top. \tag{13}$$

The time derivative and integral of any of the Fourier-approximated signals can be conveniently expressed through the block-diagonal operator $\boldsymbol{\mathcal{D}}$, defined as

$$\boldsymbol{\mathcal{D}} = \bigoplus_{n=1}^{N/2} \boldsymbol{D_n} = \bigoplus_{n=1}^{N/2} \begin{bmatrix} 0 & n\omega_0 \\ -n\omega_0 & 0 \end{bmatrix}, \tag{14}$$

where $\bigoplus$ denotes the direct sum operator. Using this representation, the position and acceleration of the WEC are approximated as

$$\boldsymbol{x}(t) \approx \tilde{\boldsymbol{x}}(t) = \mathbf{\Phi}(t)\boldsymbol{\mathcal{D}}^{-1}\boldsymbol{\mathcal{V}}, \tag{15}$$

$$\dot{\boldsymbol{v}}(t) \approx \dot{\tilde{\boldsymbol{v}}}(t) = \mathbf{\Phi}(t)\boldsymbol{\mathcal{D}}\boldsymbol{\mathcal{V}}. \tag{16}$$

Furthermore, by applying a Galerkin projection, where the dynamics are expressed in residual form and orthogonality is enforced with respect to the chosen basis [22], equation (1) can be written as:

$$\boldsymbol{\mathcal{G}_w}\boldsymbol{\mathcal{V}} = \boldsymbol{\mathcal{E}} - \boldsymbol{\mathcal{U}}, \tag{17}$$

where $\boldsymbol{\mathcal{G}}_w$ is the WEC transfer matrix, defined as

$$\boldsymbol{\mathcal{G}_w} = \bigoplus_{n=1}^{N/2} \boldsymbol{G_{w,n}} = \bigoplus_{n=1}^{N/2} \begin{bmatrix} B_w(n\omega_0) & X_w(n\omega_0) \\ -X_w(n\omega_0) & B_w(n\omega_0) \end{bmatrix}. \tag{18}$$

Here, $B_w(n\omega_0)$ and $X_w(n\omega_0)$ are the n-th elements of the WEC transfer matrix, defined as

$$B_w(n\omega_0) = B_r(n\omega_0), \tag{19}$$

$$X_w(n\omega_0) = n\omega_0 \left(m_w + m_r(n\omega_0) + m_\infty - \frac{S_h}{(n\omega_0)^2} \right), \tag{20}$$

where $B_r(\omega)$ denotes the radiation damping, while $A(\omega) = m_r(\omega) + m_\infty$ represents the added mass due to radiation effects. These hydrodynamic coefficients are typically obtained using Boundary Element Method (BEM) solvers such as NEMOH, Capytaine, or WAMIT [23]–[25].

As a result, the spectral approach enables the transcription of the infinite-dimensional continuous-time OCP (2)–(5) into the following finite-dimensional form:

$$\max.: \quad \widetilde{\mathcal{J}} = \frac{T_0}{2}\boldsymbol{\mathcal{U}}^\top \boldsymbol{\mathcal{G}_w}^{-1}\boldsymbol{\mathcal{E}} - \frac{T_0}{2}\boldsymbol{\mathcal{U}}^\top \boldsymbol{\mathcal{G}_w}^{-1}\boldsymbol{\mathcal{U}}, \tag{21}$$

$$s.t.: \ \pm\tilde{x}(t_m) = \pm\mathbf{\Phi}(t_m)\boldsymbol{\mathcal{D}}^{-1}\boldsymbol{\mathcal{G}_w}^{-1}(\boldsymbol{\mathcal{E}} - \boldsymbol{\mathcal{U}}) \leq x_{max}, \tag{22}$$

$$\pm\widetilde{F}_u(t_m) = \pm\mathbf{\Phi}(t_m)\boldsymbol{\mathcal{U}} \leq F_{u,max}, \tag{23}$$

$$\tilde{p}_u(t_m) = \boldsymbol{\mathcal{U}}^\top \mathbf{\Phi}^\top(t_m)\mathbf{\Phi}(t_m)\boldsymbol{\mathcal{G}_w}^{-1}(\boldsymbol{\mathcal{E}} - \boldsymbol{\mathcal{U}}) \geq 0, \tag{24}$$

$$\forall t_m \in \mathcal{T} = \{t_1, \ldots, t_M\} \subset [0, T_0].$$

The resulting OCP (21)–(24) seeks to determine the control coefficient vector $\boldsymbol{\mathcal{U}}$ that maximizes (21), subject to constraints (22)–(24), enforced at the discrete collocation points $t_m \in \mathcal{T} \subset [0, T_0]$.

B. Considerations for Numerical Implementation

It is worth noting that the optimization problems associated with configurations Ⓒ3 and Ⓒ4, defined by OCP (21)–(23) (excluding the power constraint), feature a quadratic objective and linear constraints with respect to $\boldsymbol{\mathcal{U}}$. These problems can therefore be efficiently solved using standard quadratic programming (QP) solvers [16], [22], [26].

In contrast, the inclusion of the unidirectional power requirement through expression (24) in configurations Ⓒ1 and Ⓒ2 introduces a nonlinear constraint, precluding the use of QP solvers and significantly increasing computational cost [16], [26]. To reduce the computational burden, analytical expressions for the gradient and Hessian of both the objective function and the nonlinear constraint can be incorporated into nonlinear

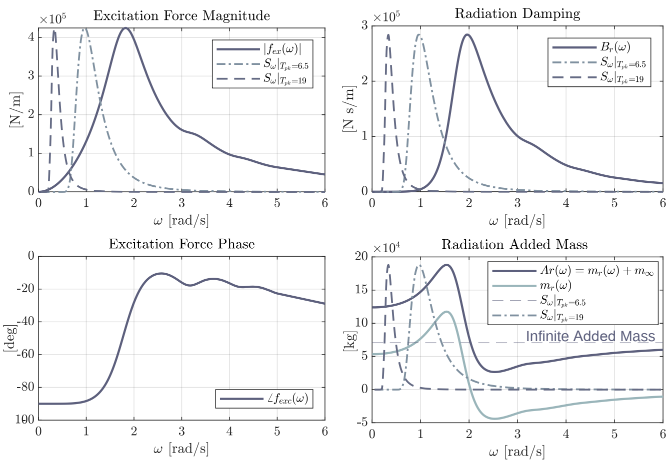

(a) (b)

Fig. 2: Hydrodynamic frequency response of the Wavepiston device. (a) Magnitude and phase of the excitation force. (b) Radiation damping and added mass. For reference, two normalized Bretschneider wave spectra (dashed lines) with peak periods $T_{pk} = \{6.5, 19\}$ s, representing the lower and upper bounds of the sea states considered in this study, are included for comparison with the hydrodynamic response.

programming (NLP) solvers. The corresponding analytical expressions, associated with OCP (21)–(24), are provided next.

The gradient of the objective function (21) with respect to the control force coefficient vector, denoted as $\nabla\widetilde{\mathcal{J}} \in \mathbb{R}^N$, is given by

$$\nabla\widetilde{\mathcal{J}} = \frac{T_0}{2}\,\boldsymbol{\mathcal{G}}_{\boldsymbol{w}}^{-1}\boldsymbol{\mathcal{E}} - \frac{T_0}{2}\left(\boldsymbol{\mathcal{G}}_{\boldsymbol{w}}^{-1} + \boldsymbol{\mathcal{G}}_{\boldsymbol{w}}^{-T}\right)\boldsymbol{\mathcal{U}}, \tag{25}$$

The corresponding Hessian of the objective function (21), $H(\widetilde{\mathcal{J}}) \in \mathbb{R}^{N\times N}$, is given by

$$H(\widetilde{\mathcal{J}}) = -\frac{T_0}{2}\left(\boldsymbol{\mathcal{G}}_{\boldsymbol{w}}^{-1} + \boldsymbol{\mathcal{G}}_{\boldsymbol{w}}^{-T}\right). \tag{26}$$

In addition, the gradient of the power constraint (24) with respect to $\boldsymbol{\mathcal{U}}$, evaluated at the collocation point t_m, denoted by $\nabla\tilde{p}_u(t_m) \in \mathbb{R}^N$, is given by

$$\begin{aligned}\nabla\tilde{p}_u(t_m) = \boldsymbol{\Phi}^\top(t_m)\boldsymbol{\Phi}(t_m)\boldsymbol{\mathcal{G}}_{\boldsymbol{w}}^{-1}(\boldsymbol{\mathcal{E}} - \boldsymbol{\mathcal{U}}) - \\ - \boldsymbol{\mathcal{G}}_{\boldsymbol{w}}^{-T}\boldsymbol{\Phi}^\top(t_m)\boldsymbol{\Phi}(t_m)\boldsymbol{\mathcal{U}}.\end{aligned} \tag{27}$$

The corresponding Hessian of the power constraint (24), $H\big(\tilde{p}_u(t_m)\big) \in \mathbb{R}^{N\times N}$, is given by

$$H\big(\tilde{p}_u(t_m)\big) = -\boldsymbol{\Phi}^\top(t_m)\boldsymbol{\Phi}(t_m)\boldsymbol{\mathcal{G}}_{\boldsymbol{w}}^{-1} - \boldsymbol{\mathcal{G}}_{\boldsymbol{w}}^{-T}\boldsymbol{\Phi}^\top(t_m)\boldsymbol{\Phi}(t_m). \tag{28}$$

The power constraints in (24) are enforced at discrete collocation points, yielding M constraints of the form $p_u(t_m) \geq 0$. Each constraint is associated with a corresponding gradient and Hessian, as defined in (27) and (28).

IV. Numerical Case Study

In this section, the numerical case study used to evaluate the four configurations summarized in Table I is described. First, the baseline Wavepiston configuration is presented, followed by the wave climate at the evaluation site and the characterization of the spectral OCP. Finally, the criterion used to define the external spring value for configurations (C2) and (C4) is outlined.

Each Wavepiston energy collector consists of a sail with a width of 8 m, height of 4 m, and depth of 0.25 m. This geometry is modelled in the BEM software Capytaine [24], assuming infinite water depth and waves propagating perpendicular to the sail. The resulting hydrodynamic frequency response is shown in Fig. 2.

Additionally, the wave climate at a potential installation site on the northern coast of Gran Canaria (approximately $28.5°$ latitude and $-15.5°$ longitude) is used to evaluate the performance of the proposed Wavepiston configurations. The wave climate is characterized using ERA5 reanalysis data based on six years of historical records [27]. The data are condensed into twelve representative sea states, defined by the following sets of peak periods and significant wave heights:

$$\mathcal{S}_{T_{pk}} = \{6.5, 10.5, 14.5, 19\},$$
$$\mathcal{S}_{H_s} = \{1.25, 2.75, 4.25\}.$$

Figure 3a presents the occurrence distribution of the considered sea states, with labels indicating the corresponding occurrence $\mathcal{O}_{ij}$, where i and j index the peak period and significant wave height from the sets $\mathcal{S}_{T_{pk}}$ and $\mathcal{S}_{H_s}$, respectively. A Bretschneider wave spectrum is assumed to generate wave realizations for each sea state when evaluating the Wavepiston configurations.

To discretize OCP (21)–(24), a cutoff frequency of $\omega_s = 20$ rad/s is used, with a total of $N/2 = 300$ frequency components. This results in a fundamental Fourier frequency of $\omega_0 = \omega_s/(N/2) = 0.67$ rad/s and a simulation time horizon of $T_0 = 2\pi/\omega_0 = 94.25$ s. This discretization provides an adequate approximation of the Wavepiston hydrodynamics shown in Fig. 2, while capturing the higher-frequency components required to represent rapid control variations. A total of $M = 601$ equally spaced collocation points are used to enforce the constraints, with the first element of the time set $\mathcal{T}$ defined as $t_1 = 0$ s. The physical constraints include a maximum stroke of $x_{max} = 2$ m and a maximum PTO control force of $F_{u,max} = 1$ MN. To obtain statistically meaningful results, 20 realizations are generated for each sea state, and the corresponding OCP is solved for each configuration, resulting in 960 simulation runs.

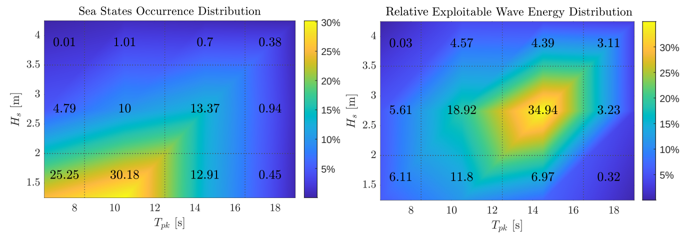

(a) (b)

Fig. 3: Wave climate at the potential deployment site in northern Gran Canaria. (a) Sea-state occurrence. (b) Relative exploitable energy.

A. Determination of the External Spring Value

As indicated in Table I, configurations (C2) and (C4) incorporate an external spring to provide restoring capability to the baseline Wavepiston configuration (C1). Determining the optimal spring value constitutes a control co-design problem, requiring iterative evaluation across the wave climate to maximize energy capture (and potentially other objectives) under multiple constraints. This challenging problem is beyond the scope of the present study. Instead, a simplified approach is adopted for this preliminary study, based on the exploitable energy distribution of the wave climate, which is sufficient to assess the impact of including an external spring in the baseline Wavepiston configuration.

Figure 3b shows the relative exploitable energy distribution within the selected wave climate, defined as

$$E_{r,exp,ij}\% = 100 \;\; E_{exp,ij} \; / \; \sum_{ij} E_{exp,ij},$$

where

$$E_{exp,ij} = \mathcal{O}_{ij} \; \rho g \int_0^\infty c_g(\omega) S_{\omega,ij}(\omega)\, d\omega$$

is the exploitable energy of sea state ij, ρ is the water density, g the gravitational acceleration, c_g the group velocity, and $S_{\omega,ij}$ the Bretschneider wave spectrum associated with the corresponding sea state.

As evidenced in Figure 3b, the exploitable energy is concentrated around the sea state $(T_{pk}, H_s) = (14.5, 2.75)$. Based on this observation, the external spring is selected such that the Wavepiston system resonates at the frequency corresponding to $T_{pk} = 14.5$ s. This results in a spring stiffness of $S_h = 2.45 \times 10^4$ N/m.

V. Results Analysis

This section presents a comparative analysis of the four Wavepiston configurations listed in Table I, evaluated under the Gran Canaria wave climate described in Section IV. The objective is to quantify how (a) the passive PTO enforcing unidirectional power flow and (b) the absence of restoring capabilities influence the following key performance metrics: (i) power capture across the considered sea states, (ii) sail stroke and (iii) PTO control force operational spaces, and (iv) energy production over the selected wave climate.

To this end, the performance of configurations (C2), (C3), and (C4) is systematically compared against the baseline configuration (C1), enabling a configuration-level assessment of their impact and supporting the evaluation of design implications.

A. Power Capture Performance Metrics

This subsection evaluates the power capture performance of configurations (C1)–(C4) across the sea states defined by $\mathcal{S}_{T_{pk}}$ and $\mathcal{S}_{H_s}$ (Section IV). The normalized mean power capture per sea state is defined as

$$\bar{P}^{(k)}_{nor,ij} = \bar{P}^{(k)}_{ij} / \bar{P}^{(k)}_{max},$$

where $\bar{P}^{(k)}_{ij}$ denotes the mean power capture at sea state ij, and $\bar{P}^{(k)}_{max}$ is the maximum mean power capture across all sea states for configuration (Ck).

The left column of Figure 4 presents the normalized power capture distribution across sea states, with text labels indicating the peak-to-mean power ratio for each case. The top-right subplot (Figure 4a$_{ii}$) provides an

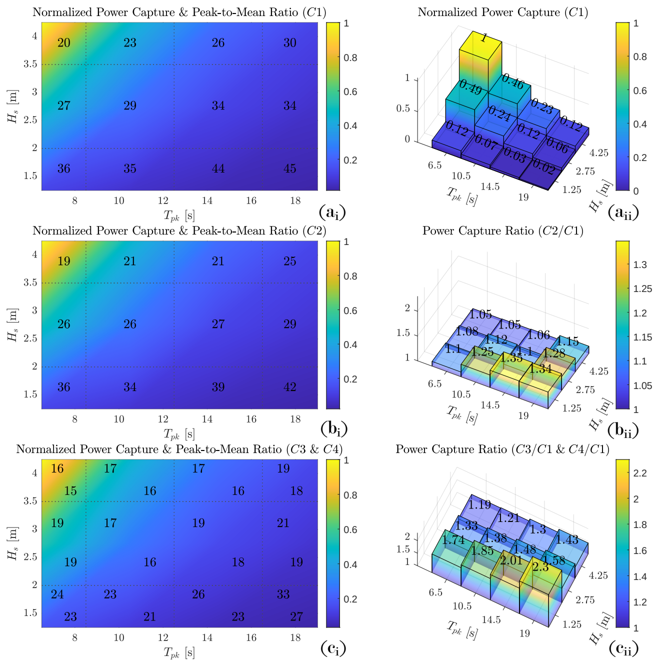

Fig. 4: Power capture performance metrics across sea states for configurations (a) (C1), (b) (C2), and (c) (C3)&(C4). Subplots (a$_i$)–(c$_i$) show the normalized power capture, with labels indicating the corresponding peak-to-mean power ratio. Subplot (a$_{ii}$) presents a bar representation of the normalized power capture for (C1), while subplots (b$_{ii}$)–(c$_{ii}$) show the power capture ratio of (C2) and (C3)&(C4) relative to (C1).

equivalent bar representation of the normalized power capture for the baseline configuration (C1). The lower-right subplots (Figures 4b$_{ii}$ and 4c$_{ii}$) show the power capture ratios relative to (C1), defined as $\bar{P}^{(k)}_{ij}/\bar{P}^{(1)}_{ij}$, and denoted as $(Ck/C1)$.

Configurations (C3) and (C4), which incorporate a reactive PTO, exhibit identical normalized power capture distributions, regardless of the presence of an external spring. However, their peak-to-mean power ratios differ, as indicated by the two text labels shown in Figure 4c$_i$: the upper-left label corresponds to configuration (C3), while the lower-right label corresponds to (C4). These differences arise from the distinct control force requirements in the two configurations and are further discussed in Section V-C.

Across all configurations, the power capture distribution exhibits a consistent trend: higher values are obtained for shorter peak periods and larger significant wave heights. This behavior is primarily driven by the hydrodynamic frequency response of the device (Figure 2), where larger excitation force magnitudes occur at higher frequencies corresponding to shorter-period sea states. This contrasts with typical heave point absorbers, which exhibit peak excitation at lower frequencies [28].

From a configuration perspective, both the addition of a restoring force ((C2)) and the introduction of a reactive PTO ((C3), (C4)) lead to improvements in power capture relative to the baseline configuration ((C1)), see Figure 4b$_{ii}$ and 4c$_{ii}$. However, the magnitude and nature of these improvements differ significantly.

The inclusion of an external spring (C2) yields moderate gains, particularly at longer peak periods and lower wave heights. In contrast, configurations with a reactive PTO (C3, C4) achieve substantially higher improvements, with power capture increases of up to 2.3 times that of the baseline configuration for certain sea states.

However, the power capture ratios (Ck/C1) shown in Figures 4b$_{ii}$ and 4c$_{ii}$ indicate that the largest relative improvements occur in sea states where the baseline configuration C1 exhibits low normalized power capture. In other words, the ratios increase in regions where the baseline performance decreases. As a result, even large relative gains do not translate into significant improvements in overall performance. When averaged across all sea states, the mean power capture with respect to C1 increases by only 8% for C2, compared to 32% for C3 and C4.

From a design perspective, these results highlight that enabling bidirectional power flow through a reactive PTO is the primary driver for improving power capture performance, while the introduction of restoring capabilities provides comparatively limited benefits.

B. Stroke Performance Metrics

This subsection evaluates the stroke performance of configurations C1–C4 in terms of the root-mean-square (RMS) sail position, denoted as $x^{(k)}_{rms,ij}$, where k and ij indicate the configuration and sea state, respectively.

The left column of Figure 5 presents the RMS position distribution across sea states, with text labels indicating the peak values reached in each case. The top-right subplot (Figure 5a$_{ii}$) provides a bar representation of the RMS position for the baseline configuration C1, while the lower-right subplots (Figures 5b$_{ii}$ and 5c$_{ii}$) show the RMS position ratios relative to C1, defined as $x^{(k)}_{rms,ij}/x^{(1)}_{rms,ij}$, and denoted as $(Ck/C1)$. Configurations C3 and C4, which incorporate a reactive PTO, exhibit identical RMS position distributions regardless of the presence of an external spring, and are therefore plotted together in Figure 5c.

For all configurations, a consistent trend is observed in the left column of Figure 5: the RMS position varies more strongly with significant wave height than with peak period across the evaluated sea states, increasing with larger wave heights. Additionally, the peak position labels indicate that the allowable stroke limit is reached in all sea states across all configurations.

From a configuration perspective, both the addition of a restoring force (C2) and the introduction of a reactive PTO (C3, C4) increase the RMS position relative to the baseline C1. The inclusion of an external spring (C2) leads to moderate increases in motion. In contrast, configurations with a reactive PTO (C3, C4) exhibit a more pronounced amplification of motion across the sea states, resulting in consistently higher RMS position levels.

Moreover, the RMS position ratios show that changes in the motion operational space vary across configurations differently. In particular, configuration C2

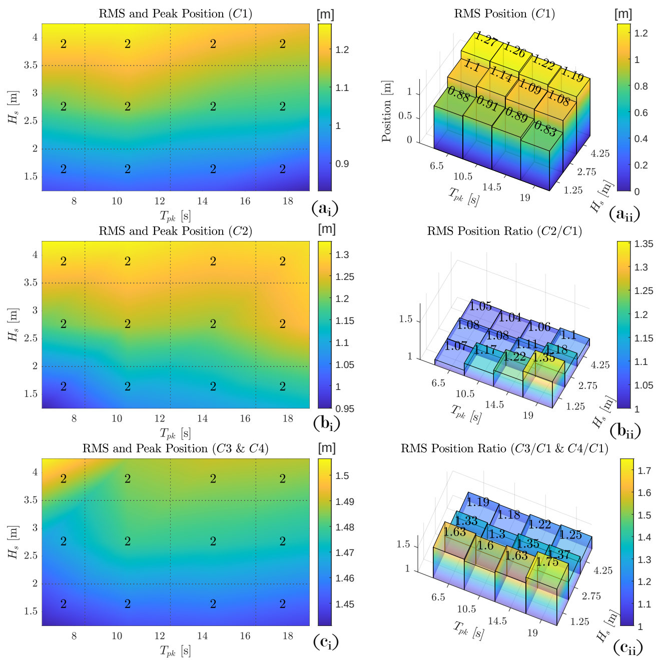

Fig. 5: Sail stroke performance metrics across sea states for configurations (a) C1, (b) C2, and (c) C3&C4. Subplots (a$_i$)–(c$_i$) show the RMS position, with labels indicating the corresponding peak values. Subplot (a$_{ii}$) presents a bar representation of the RMS position for C1, while subplots (b$_{ii}$)–(c$_{ii}$) show the RMS position ratio of C2 and C3&C4 relative to C1.

exhibits increases in RMS position that become more pronounced with increasing peak period and decreasing wave height (Figure 5b$_{ii}$). In contrast, configurations with a reactive PTO (C3, C4) exhibit a milder variation across peak periods, with a subtle minimum around $T_{pk} = 10.5$ s, while displaying a more pronounced dependence on significant wave height (Figure 5c$_{ii}$).

From a design perspective, these results highlight a key trade-off: while reactive PTO control significantly enhances power capture, it also leads to increased motion amplitudes. This amplification of stroke may impose stricter mechanical and structural requirements on the device. In contrast, the addition of a restoring force results in more moderate increases in motion, consistent with its comparatively limited impact on power capture, and may therefore represent a more conservative design modification.

C. PTO Control Force Performance Metrics

This subsection evaluates the control force performance of configurations C1–C4 in terms of the RMS PTO force, denoted as $F^{(k)}_{u,rms,ij}$, where k and ij indicate the configuration and sea state, respectively.

The left column of Figure 6 presents the RMS control force distribution across sea states, with text labels indicating the peak force values for each sea state. The top-right subplot (Figure 6a$_{ii}$) provides a bar representation of the RMS control force for the baseline configuration C1, while the remaining subplots (Figures 6b$_{ii}$–6d$_{ii}$) show the RMS force ratios relative to C1, defined as $F^{(k)}_{u,rms,ij}/F^{(1)}_{u,rms,ij}$, and denoted as $(Ck/C1)$.

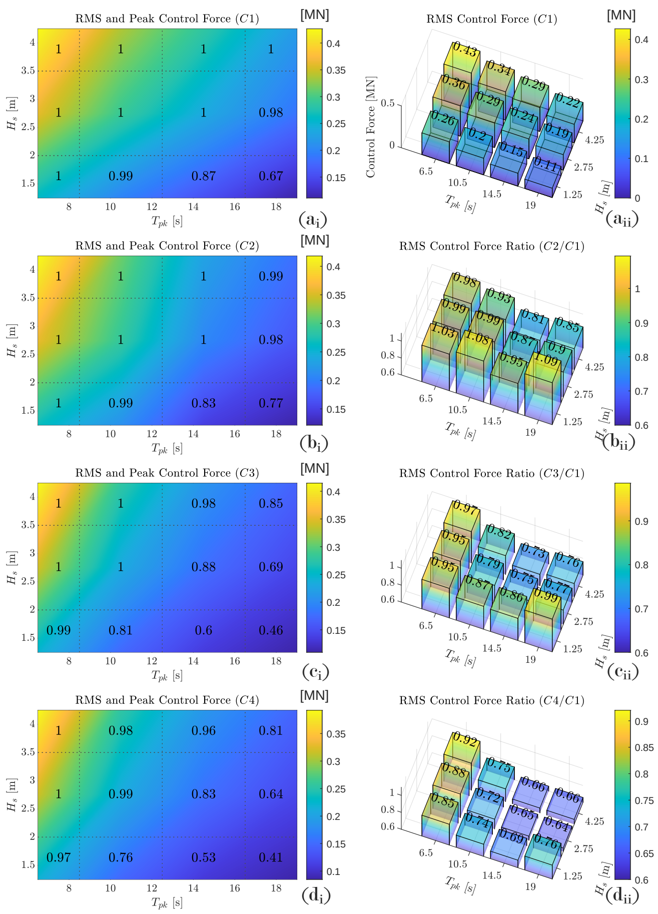

Fig. 6: PTO control force performance metrics across sea states for configurations (a) C1, (b) C2, (c) C3, and (d) C4. Subplots (a$_i$)–(d$_i$) show the RMS control force, with labels indicating the corresponding peak values. Subplot (a$_{ii}$) presents a bar representation of the RMS control force for C1, while subplots (b$_{ii}$)–(d$_{ii}$) show the RMS control force ratio of C2, C3, and C4 relative to C1.

Across all configurations, a consistent trend is observed in the left column of Figure 6: the RMS control force increases for shorter peak periods and larger significant wave heights. In contrast to the stroke constraint, the control force limits are not reached across all sea states; specifically, they remain inactive across the different configurations for sea states with larger peak periods and lower wave heights.

From a configuration perspective, the addition of an external spring (C2) reduces the RMS control force relative to the baseline C1 in most sea states (Figure 6b$_{ii}$). This reduction is most pronounced around $T_{pk} = 14.5$ s, where the spring is tuned to introduce a resonant response of the device.

Configurations incorporating a reactive PTO (C3, C4) further reduce the required control force across the sea states, as shown in Figures 6c$_{ii}$ and 6d$_{ii}$. These configurations exhibit lower RMS and peak control force levels than the baseline case, with configuration C4 achieving the lowest values overall. The RMS force ratios display a non-uniform distribution across peak periods, with a local minimum around $T_{pk} = 14.5$ s and increasing values towards both lower and higher peak periods.

A key result emerges from this analysis: both the inclusion of an external spring and the introduction of a reactive PTO reduce the required control force relative to the baseline configuration, with the reactive PTO providing the most significant reduction across all sea states. This improvement occurs alongside increased power capture across all configurations, at the cost of increased motion amplitudes, as discussed in Sections V-A and V-B, respectively.

From a design perspective, configuration C4, which combines reactive control with restoring capabilities, provides the most favorable control force performance among the configurations considered, achieving the lowest RMS and peak force levels across the sea states.

D. Energy Production Performance Metrics

The final performance metric evaluates the relative energy production per sea state, defined as

$$E^{(k)}_{r,ij}\% = 100\, \mathcal{O}_{ij}\, \bar{P}^{(k)}_{ij} / E^{(k)}_T,$$

where k denotes the configuration, ij the sea state, and $E^{(k)}_T = \sum_{ij} \mathcal{O}_{ij} \bar{P}^{(k)}_{ij}$ represents the total energy production for the given wave climate. Note, the relative energy production metric reflects the contribution of each sea state by weighting its mean power capture ($\bar{P}^{(k)}_{ij}$) with its corresponding occurrence ($\mathcal{O}_{ij}$).

The left column of Figure 7 presents the relative energy production distribution across sea states. Configurations C3 and C4 exhibit identical energy production distributions and are therefore presented together. The top-right subplot (Figure 7a$_{ii}$) provides a bar representation of the relative energy production for configuration C1, while the lower-right subplots (Figures 7b$_{ii}$ and 7c$_{ii}$) show the variations in relative energy production with respect to C1 for each sea state, defined as

$$\Delta E^{(k)}_{r,ij}\% = E^{(1)}_{r,ij}\% \left(\mathcal{O}_{ij}\, \bar{P}^{(k)}_{ij} / \mathcal{O}_{ij}\, \bar{P}^{(1)}_{ij} - 1 \right),$$

where k and ij denote the configuration and sea state, respectively. Furthermore, the total variation in energy production with respect to C1 for configuration k is obtained by summing the contributions across all sea states as

$$100 \left(E^{(k)}_T - E^{(1)}_T \right) / E^{(1)}_T = \sum_{ij} \Delta E^{(k)}_{r,ij}\%,$$

which provides a consistent link between the local variations per sea state and the overall change in energy production across the wave climate.

Across all configurations, the relative energy production is concentrated in sea states characterized by shorter peak periods and lower significant wave heights (Figure 7a$_i$–c$_i$). This distribution closely follows the occurrence of the wave climate (Figure 3a), indicating that the most frequently occurring sea states dominate the overall energy production. As a result, sea states characterized by shorter peak periods and lower significant wave heights—despite exhibiting relatively low normalized power capture (see Figure 4)—contribute most to the overall energy production due to their high occurrence.

From a configuration perspective, the addition of an external spring (C2) produces moderate changes in

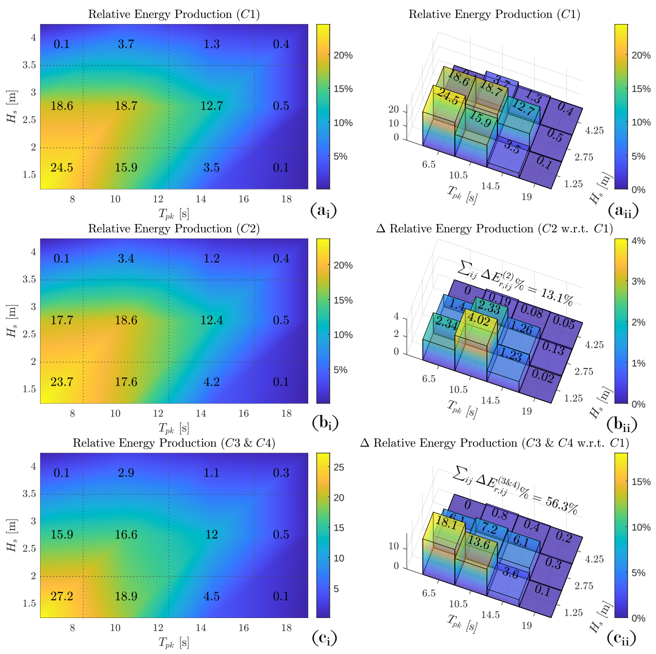

Fig. 7: Energy production performance metrics across sea states for configurations (a) (C1), (b) (C2), and (c) (C3)&(C4). Subplots (a_i)–(c_i) show the relative energy production. Subplot (a_{ii}) presents a bar representation of the relative energy production for (C1), while subplots (b_{ii})–(c_{ii}) show the percentage variation in energy production of (C2) and (C3)&(C4) relative to (C1).

the relative energy distribution across sea states (Figure 7b_{ii}). While local increases are observed, the dominant contribution remains associated with the most frequent sea states. This corresponds to an increase in total energy production of approximately 13% relative to the baseline configuration.

In contrast, configurations incorporating a reactive PTO ((C3), (C4)) lead to more significant variations in relative energy production across sea states than configuration (C2) (Figure 7c_{ii}). The largest increases occur in the most frequently occurring sea states, resulting in a stronger concentration of energy production in this region in comparison to (C1). Overall, these configurations achieve a substantially higher increase in total energy production, approximately 56% relative to (C1).

A key result emerges from this analysis: improvements in power capture do not translate uniformly into energy production gains, as the contribution of each sea state is dominated—at least within the Gran Canaria wave climate considered—by its occurrence.

From a design perspective, the device could potentially be configured to exploit the sea states that contribute most to the overall energy production within a given wave climate. For the Wavepiston configurations analyzed under the Gran Canaria wave climate, the sea states contributing most to total energy production are primarily the most frequently occurring ones, rather than those associated with the highest power capture. This suggests that design choices—such as the inclusion of restoring capabilities or the adoption of a reactive PTO—could be guided by performance under these energy-dominant sea states.

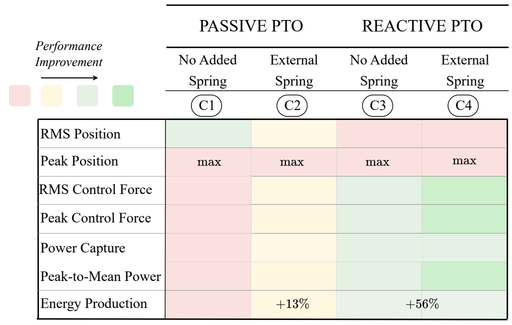

Fig. 8: Condensed comparison of performance metrics across Wavepiston configurations. The red–yellow–green color scale indicates relative performance for each metric, with green denoting the best performance.

E. Technology Development Implications

When evaluating potential design pathways for the Wavepiston device, important trade-offs emerge between the different performance metrics. While increasing energy production remains a primary objective, improvements in this metric are inherently linked to variations in motion amplitude, control force requirements, and peak-to-mean power ratios.

Variations across the different performance metrics have direct implications for the physical design and operation of the device. Increased motion amplitudes may lead to operation closer to stroke limits, potentially affecting structural integrity and reliability. Similarly, larger control force requirements can impose stricter demands on PTO sizing and actuation capabilities. In addition, high peak-to-mean power ratios may require over-dimensioning of PTO components, with associated impacts on system complexity and cost.

To synthesize the multi-metric trade-offs across the four configurations analyzed in this study and to support the interpretation of their technological implications, Figure 8 is introduced. This figure compares the performance of each configuration for each metric using a color-coded scale, thereby enabling a direct visual assessment of how the inclusion of an external spring and/or a reactive PTO influences the different performance metrics. The color scale ranges from red to green, indicating lower to higher performance, respectively, across the evaluated metrics.

1) Implications of Integrating an External Spring: The addition of an external spring in configuration (C2) introduces restoring capabilities that result in moderate changes across the evaluated metrics. In particular, it leads to a slight increase in RMS position across all sea states, while reducing the RMS control force for most sea states, with minimal impact on peak force levels, consistent with the performance trends summarized in Figure 8.

Although improvements in power capture are observed for configuration (C2) relative to the baseline configuration (C1), these are primarily concentrated in sea states where (C1) exhibits lower power capture and that do not correspond to the most frequently occurring sea states. As a result, the improvements in power capture at these sea states do not translate into a significant contribution to the overall energy production, leading to an increase of approximately 13% relative to C1. Overall, the addition of an external spring yields moderate and balanced improvements across the evaluated metrics, without significantly increasing the overall energy production of the device (see Figure 8).

2) Implications of Integrating a Reactive PTO: The introduction of a reactive PTO in configurations C3 and C4 results in significant changes across the evaluated metrics. In particular, both RMS and peak control forces are reduced relative to the baseline configuration, with C4—which combines a reactive PTO with an external spring—achieving the lowest force levels among all configurations. In addition, reactive PTO configurations yield the highest power capture across sea states together with reduced peak-to-mean power ratios, resulting in the largest increase in total energy production, approximately 56% relative to C1.

Overall, the introduction of a reactive PTO leads to substantial improvements in power capture, control force requirements, and energy production, at the cost of increased motion amplitudes, as reflected in the performance trends summarized in Figure 8.

3) Cross-Metric Trade-offs: The results presented in the previous subsections highlight inherent interdependencies between the evaluated performance metrics, revealing trade-offs that must be considered when assessing design alternatives. In particular, modifications to the Wavepiston configuration, including the integration of an external spring or a reactive PTO, lead to coupled variations in motion amplitude, control force requirements, and energy production, rather than affecting individual metrics independently. In this context, the presentation of performance metrics across sea states (Figures 4–7), together with the condensed summary in Figure 8, facilitates the identification of these trade-offs by enabling both detailed and comparative analysis across configurations and metrics.

As a result, the selection of a given configuration cannot be based on a single performance metric, but must instead account for the relative importance of motion constraints, actuator requirements, and energy production within the intended operational context. Overall, these findings emphasize the need for a multi-metric perspective in the design and evaluation of Wavepiston configurations. Moreover, the performance results should be considered alongside broader technological implications, including economic factors, reliability considerations, and aspects influencing the levelized cost of energy (LCOE). Although such analyses are beyond the scope of this work, the results presented here provide a structured basis for informing future design and technology development decisions.

4) Considerations for the Interpretation of the Results: While the present study provides a comprehensive comparison of performance metrics across Wavepiston configurations, a number of modeling assumptions should be considered when interpreting the results.

First, the hydrodynamic model is linear and does not account for nonlinear effects such as viscous drag, which may influence both motion and power capture. Furthermore, the PTO is modeled as ideal, neglecting its dynamics and mechanical-to-electrical conversion losses. These assumptions are particularly relevant for configurations C3 and C4, which incorporate reactive PTO control and exhibit the most favorable performance across the evaluated metrics.

In practice, implementing reactive control requires bidirectional power exchange between the PTO and WEC, involving continuous power flow through the conversion system. This power exchange is subject to conversion losses, reducing the energy delivered by the device and potentially limiting the effective gains in power capture achieved through reactive control [29].

Consequently, although the results provide valuable insights into the comparative performance of different configurations, the quantitative outcomes should be interpreted with caution, as the modeling assumptions may influence both the control strategy effectiveness and the resulting energy production.

VI. Conclusions

This study presents a multi-metric performance assessment of the Wavepiston device, focusing on the impact of two key baseline design characteristics: the unidirectional power flow of its passive PTO and the absence of restoring capabilities. To evaluate the influence of these characteristics on device performance, three alternative configurations are considered and compared against the baseline configuration C1: C2, which includes an external spring providing restoring capabilities, and C3 and C4, which implement a reactive PTO enabling bidirectional power flow, with and without an external spring, respectively.

For each configuration, the optimal control problem is solved for every sea state within the wave climate of a potential deployment site in northern Gran Canaria using a spectral control approach. Importantly, this work also provides insights into reducing the computational burden associated with solving the OCP under nonlinear power constraints, particularly for configurations incorporating a passive PTO. The resulting case study enables the evaluation of key performance metrics across the four Wavepiston configurations (C1–C4), including (i) power capture across sea states, (ii) stroke and (iii) PTO control force operational spaces, and (iv) energy production over the considered wave climate.

The results are presented in two complementary forms: detailed distributions across sea states (Figures 4–7) and a condensed representation summarizing the performance of each configuration across all metrics (Figure 8). This combined presentation enables both detailed analysis at the level of individual sea states within the considered wave climate and a concise visual summary that facilitates the assessment of performance trends and supports the evaluation of potential design pathways.

In particular, the introduction of a reactive PTO to the Wavepiston baseline configuration yields the most pronounced improvements across nearly all evaluated performance metrics, achieving the largest gains in power capture across individual sea states and in total energy production within the considered wave climate (approximately 56% relative to (C1)), while simultaneously reducing control force requirements and peak-to-mean power ratio. These improvements, however, come at the cost of a significant increase in stroke operational space, resulting in operation closer to the stroke end stops and potentially increasing structural and reliability risks. In contrast, the addition of an external spring leads to more moderate and balanced improvements, with a comparatively limited impact on overall energy production (approximately 13% relative to (C1)), while also resulting in a less pronounced increase in motion amplitude.

Moreover, the analysis shows that energy production across all configurations is strongly influenced by the occurrence of sea states within the considered wave climate. As a consequence, improvements in power capture in less frequent sea states do not translate proportionally into increases in total energy production. From a design perspective, this indicates that system parameters, such as the tuning of the external spring, may be selected to enhance performance in the most frequently occurring sea states, which contribute most to overall energy production within the considered wave climate.

Overall, the results obtained in this study provide a structured basis for identifying inherent performance trade-offs and their dependence on the wave climate under consideration, extending beyond those explicitly discussed herein. Furthermore, from a design perspective, the interdependence between performance metrics, as evidenced by the results presented in Figures 4–8, indicates that design pathways should be evaluated using a multi-metric approach that accounts for the interplay between energy production, motion constraints, actuator requirements, and the occurrence of sea states at the target deployment site.

Finally, while this study focuses on the evaluation of performance metrics across different Wavepiston configurations without explicitly addressing techno-economic aspects, it provides a structured foundation for future research in this direction. In particular, extending the analysis to assess the impact of design choices on the LCOE represents a key next step. In addition, the analysis highlights the relevance of a control co-design approach, integrating electro-mechanical characteristics of the WEC with control design to further improve overall system performance, constituting a promising pathway for further investigation.

References

[1] WavePiston, "Wavepiston official website," (accessed April 18, 2025). [Online]. Available: https://wavepiston.dk/

[2] PLOCAN, "Wavepiston experimental test at plocan," accessed April 18, 2025. [Online]. Available: https://plocan.eu/en/projects/wavepiston-competitive-wave-energy-on-islands

[3] B. Joensen and H. B. Bingham, "Economic feasibility study for wave energy conversion device deployment in faroese waters," *Energy*, vol. 295, p. 130869, 5 2024.

[4] J. Schallenberg-Rodríguez, B. D. Rio-Gamero, N. Melian-Martel, T. L. Alecio *et al.*, "Energy supply of a large size desalination plant using wave energy. practical case: North of gran canaria," *Applied Energy*, vol. 278, p. 115681, 11 2020.

[5] B. D. Río-Gamero, T. L. Alecio, and J. Schallenberg-Rodríguez, "Performance indicators for coupling desalination plants with wave energy," *Desalination*, vol. 525, p. 115479, 3 2022.

[6] K. M. Brodersen, E. A. Bywater, A. M. Lanter, H. H. Schennum *et al.*, "Direct-drive ocean wave-powered batch reverse osmosis," *Desalination*, vol. 523, p. 115393, 2 2022.

[7] O. Choupin, M. Henriksen, A. Etemad-Shahidi, and R. Tomlinson, "Breaking-down and parameterising wave energy converter costs using the capex and similitude methods," *Energies*, vol. 14, p. 902, 2 2021.

[8] O. Choupin, "A methodology to asses suitable wave energy converter and location pairing," Ph.D. dissertation, Griffith University, 2021.

[9] O. Choupin, A. Têtu, B. D. Río-Gamero, F. Ferri *et al.*, "Premises for an annual energy production and capacity factor improvement towards a few optimised wave energy converters configurations and resources pairs," *Applied Energy*, vol. 312, p. 118716, 4 2022.

[10] B. D. Río-Gamero, O. Choupin, N. Melián-Martel, and J. Schallenberg-Rodriguez, "Application of a revised integration of methods for wave energy converter and farm location pair mapping," *Energy Conversion and Management*, vol. 303, p. 118170, 3 2024.

[11] O. Choupin, F. P. Andutta, A. Etemad-Shahidi, and R. Tomlinson, "A decision-making process for wave energy converter and location pairing," *Renewable and Sustainable Energy Reviews*, vol. 147, p. 111225, 9 2021.

[12] O. Choupin, M. Henriksen, and R. Tomlinson, "Interrelationship between variables for wave direction-dependent wec/site-configuration pairs using the capex method," *Energy*, vol. 248, p. 123552, 6 2022.

[13] A. Pecher, J. Kofoed, and E. Angelelli, *Experimental Study on the WavePiston Wave Energy Converter*, ser. DCE Contract Reports, no. 73. Denmark: Department of Civil Engineering, Aalborg University, 2010.

[14] E. Angelelli, B. Zanuttigh, J. Kofoed, and K. Glejbøl, "Experiments on the wavepiston, wave energy converter," in *9th ewtec 2011*, A. Bahaj, Ed. University of Southampton, 2011, published on a cd.; The 9th European Wave and Tidal Energy Conference : EWTEC 2011 ; Conference date: 05-09-2011 Through 09-09-2011.

[15] R. Read and H. Bingham, "Time- and frequency-domain comparisons of the wavepiston wave energy converter," 2018, 33rd International Workshop on Water Waves and Floating Bodies (IWWWFB 2018); 04-04-2018 Through 07-04-2018.

[16] N. Faedo, S. Olaya, and J. V. Ringwood, "Optimal control, MPC and MPC-like algorithms for wave energy systems: An overview," *IFAC J. Syst. Control*, vol. 1, pp. 37–56, Sep. 2017.

[17] U. A. Korde and J. Ringwood, *Hydrodynamic Control of Wave Energy Devices*. Cambridge University Press, Sep. 2016.

[18] J. V. Ringwood, G. Bacelli, and F. Fusco, "Energy-maximizing control of wave-energy converters: The development of control system technology to optimize their operation," *IEEE Control Systems*, vol. 34, pp. 30–55, 2014.

[19] B. Guo and J. V. Ringwood, "A review of wave energy technology from a research and commercial perspective," *IET Renew. Power Gener.*, vol. 15, no. 14, pp. 3065–3090, Oct. 2021.

[20] J. V. Ringwood, "Wave energy control: status and perspectives 2020," *IFAC-PapersOnLine*, vol. 53, pp. 12 271–12 282, 2020.

[21] L. Wang, J. Isberg, and E. Tedeschi, "Review of control strategies for wave energy conversion systems and their validation: the wave-to-wire approach," *Renew. Sustain. Energy Rev.*, vol. 81, pp. 366–379, Jan. 2018.

[22] G. Bacelli and J. V. Ringwood, "Numerical Optimal Control of Wave Energy Converters," *IEEE Trans. Sustain. Energy*, vol. 6, no. 2, pp. 294–302, Apr. 2015.

[23] A. Babarit and G. Delhommeau, "Theoretical and numerical aspects of the open source BEM solver NEMOH," in *11th Eur. Wave Tidal Energy Conf.*, Nantes, France, 2015.

[24] M. Ancellin and F. Dias, "Capytaine: a python-based linear potential flow solver," *Journal of Open Source Software*, vol. 4, p. 1341, 4 2019.

[25] C. Lee and J. Newman, "Wamit user manual," p. 343, 2006.

[26] J. T. Betts, *Practical Methods for Optimal Control and Estimation Using Nonlinear Programming*. Society for Industrial and Applied Mathematics, 1 2010.

[27] H. Hersbach, B. Bell, P. Berrisford, S. Hirahara *et al.*, "The era5 global reanalysis," *Quarterly Journal of the Royal Meteorological Society*, vol. 146, pp. 1999–2049, 7 2020.

[28] J. Falnes and A. Kurniawan, *Ocean Waves and Oscillating Systems*. Cambridge University Press, May. 2020.

[29] R. Genest, F. Bonnefoy, A. H. Clément, and A. Babarit, "Effect of non-ideal power take-off on the energy absorption of a reactively controlled one degree of freedom wave energy converter," *Applied Ocean Research*, vol. 48, pp. 236–243, 10 2014.